Self-consistent generation of the ambipolar electric field in collisionless plasmas via multi-mode electrostatics

Luca Barbieri[1,2]

[1]CNRS - LIRA - Paris Observatory - Meudon Site, Meudon, France
[2]Sorbonne University, Paris, France
Corresponding author: Luca Barbieri, luca.barbieri@obspm.fr

In this work, we investigate the generation of the ambipolar electric field in a gravitationally stratified, collisionless plasma atmosphere. In such environments, gravity tends to separate charged species. To prevent separation an electric field, classically described by the Pannekoek–Rosseland expression, is usually imposed externally. Here, we propose a self-consistent method to recover this field based on a multi-mode Fourier expansion of the electrostatic interaction. We show that, under suitable conditions, this approach naturally leads to the ambipolar electric field and restores charge neutrality. The method is tested in both isothermal and multi-temperature plasma configurations. This framework provides a foundation for future developments that may include collisions, ionisation and asymmetric boundary conditions to model more realistic stellar atmospheres.

Key words: plasma dynamics, plasma nonlinear phenomena, plasma properties

---

1. Introduction

In the solar corona, the outermost layer of the solar atmosphere, the temperature rises from thousands to millions of degrees with increasing altitude, while the density simultaneously drops by more than two orders of magnitude. Understanding how the coronal plasma achieves this stationary configuration remains a fundamental and unresolved issue, commonly known as the coronal heating problem (Parker 1972; Ionson 1978; Heyvaerts & Priest 1983; Scudder 1992*a*, *b*; Dmitruk & Gomez 1997; Gudiksen & Nordlund 2005; Rappazzo *et al.* 2008; Pontieu *et al.* 2011; Rappazzo & Parker 2013; Wilmot-Smith 2015; Howson, De Moortel & Reid 2020; Hau *et al.* 2025).

The upper chromosphere and the base of the transition region are known to be highly dynamic, characterised by intense, short-lived and small-scale brightenings (Dere, Bartoe & Brueckner 1989; Teriaca *et al.* 2004; Peter *et al.* 2014; Tiwari *et al.* 2019; Berghmans *et al.* 2021).

Prompted by these observational evidences, recently a new kinetic model of the solar atmosphere has been proposed (Barbieri *et al.* 2024*a*, *b*), demonstrating,

through both numerical and analytical techniques, that suitable, rapid and random temperature perturbations in the upper chromosphere can drive the overlying plasma towards a stationary configuration exhibiting the observed inverted temperature and density profiles (often referred to as temperature inversion).

In this model, the coronal plasma is represented as a one-dimensional, collision-less, two-species system subject to constant downward gravity and an electric field (the Pannekoek–Rosseland field) generated by the Sun to ensure charge neutrality (Pannekoek 1922; Rosseland 1924). As pointed out in Barbieri *et al.* (2024*a*, *b*) and Barbieri, Andrea & Simone (2025), the most significant weakness of this approach lies in its omission of Coulomb collisions, despite the low Knudsen number ($K_n \sim 10^{-2} - 10^{-3}$ in the transition region and $K_n \sim 10^{-1}$ in the corona), which indicates that collisions are non-negligible in both regions.

As shown by Landi & Pantellini (2001) via numerical simulations, Coulomb collisions modify the electric field in such a way that the standard Pannekoek–Rosseland field is no longer sufficient to maintain charge neutrality. Instead, a supplementary contribution from the plasma's self-consistent electrostatic field is required. In Barbieri *et al.* (2024*a*, *b*), electrostatic interactions were approximated using the Hamiltonian mean-field (HMF) model (Antoni & Ruffo 1995; Chavanis, Vatteville & Bouchet 2005; Elskens & Escande 2019), which truncates the Fourier expansion of the electrostatic potential at the first mode.

Therefore, in order to introduce collisions into the model, it is first necessary to understand whether the HMF-based modelling developed in this work is capable of reproducing the ambipolar effect. For this reason, we do not include collisions in the present study where we focus on the collisionless limit. Our aim is to determine what form of the self-generated electric field is required to induce the ambipolar effect that leads to the Pannekoek–Rosseland field, without imposing it externally as done in previous works (Barbieri *et al.* 2024*a*, *b*; Barbieri *et al.* 2025). We show that by retaining an increasing number of Fourier modes in the electrostatic potential, it is possible to recover the ambipolar effect and thus the Pannekoek–Rosseland field in a fully self-consistent manner. This framework provides the basis for including ambipolar effects in plasma atmospheres and will support future extensions of the model, such as the inclusion of collisions.

The structure of the paper is as follows. Section 2 revisits the inadequacy of the Pannekoek–Rosseland field in ensuring charge neutrality in a collisional plasma out of thermal equilibrium. Section 3 introduces the coronal loop model from Barbieri *et al.* (2024*a*, *b*), extended to include multiple electric field modes. Section 4 shows both theoretically and numerically how the ambipolar electric field can be generated by this approach. Finally, § 5 summarises our findings and outlines potential future directions.

2. Charge neutrality in a gravitationally stratified stellar atmosphere

We consider a plane-parallel atmosphere composed of a plasma of electrons and protons stratified by the gravitational field. For each species, the hydrostatic equilibrium condition is expressed as

$$\frac{\mathrm{d}P_\alpha}{\mathrm{d}z} = n_\alpha F_\alpha, \quad F_\alpha = \mathrm{sign}(e_\alpha)eE - gm_\alpha, \quad (2.1)$$

where $\alpha \in \{e, p\}$ denotes the species (electrons or protons), m_α is the mass of a particle of species α, e is the elementary charge, g is the gravitational acceleration, z is the height, n_α is the number density, P_α is the pressure, F_α is the total force
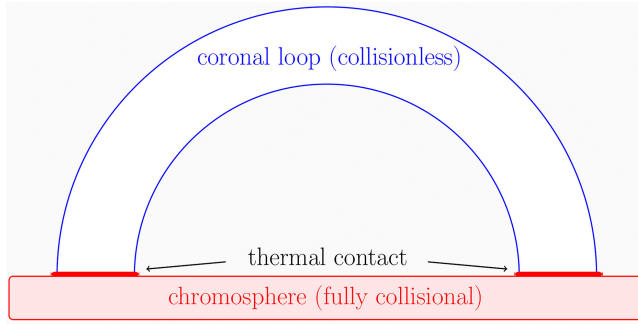
FIGURE 1. Schematics of the loop model. The coronal plasma in the loop is treated as collisionless and in thermal contact with a fully collisional chromosphere (modelled as a thermal boundary).

per unit volume, E is the electric field and R_α is the friction force due to collisions. Using the ideal gas law $P_\alpha = n_\alpha k_B T$, and assuming quasi-neutrality, $n_e(z) = n_p(z) = n(z) \, \forall z$, and the equality of temperatures, $T_e(z) = T_p(z) = T(z) \, \forall z$, we subtract the equilibrium equations for each species to isolate the electric field:

$$E = E_{\mathrm{PR}} - \frac{1}{2ne} \sum_{\alpha \in \{e,p\}} \mathrm{sign}\,(e_\alpha)\, R_\alpha + \frac{1}{2ne} \sum_{\alpha \in \{e,p\}} \mathrm{sign}\,(e_\alpha)\, \frac{\mathrm{d}\,(T_\alpha n)}{\mathrm{d}z}, \qquad (2.2)$$

where E_{PR} is the Pannekoek–Rosseland field defined as

$$E_{\mathrm{PR}} = -\frac{(m_p - m_e)}{2e} g. \qquad (2.3)$$

Even if the electron and proton temperatures are equal, the system may not be in thermal equilibrium, and thus $R_\alpha \neq 0$ due to collisional effects. Therefore, the total electric field must include an additional ambipolar contribution to restore charge neutrality. Taking the divergence of the electric field yields

$$\frac{\mathrm{d}E}{\mathrm{d}z} = \frac{1}{2e} \frac{\mathrm{d}}{\mathrm{d}z} \left[\frac{1}{n} \sum_{\alpha \in \{e,p\}} \mathrm{sign}\,(e_\alpha) \left(\frac{\mathrm{d}(T_\alpha n)}{\mathrm{d}z} - R_\alpha \right) \right], \qquad (2.4)$$

indicating that a self-consistent, spatially varying electric field must arise from the plasma to sustain quasi-neutrality. This ambipolar electric field becomes essential when collisional terms are included, as the classical Pannekoek–Rosseland field alone is insufficient. Given that Barbieri *et al.* (2024*a*, *b*) utilise the HMF model to approximate electrostatic interactions, a key question arises: can the HMF model, which retains only the first Fourier mode, reproduce the ambipolar effect and maintain charge neutrality in the presence of gravity? If not, can the model be suitably modified to include such effects by extending the Fourier mode expansion?

3. The two-component gravitationally bound plasma model

We consider geometrically confined plasma structures, specifically coronal loops, which are prevalent throughout the solar atmosphere (e.g. Aschwanden 2005). Each loop is modelled as a semicircular tube of length $2L$ and cross-sectional area S (figure 1). The plasma inside the loop is treated as a one-dimensional, collisionless,

two-species electrostatic system subject to solar gravity. The electrostatic interaction is modelled via a multi-mode Fourier expansion of the potential, truncated at a chosen mode N_n, while enforcing central symmetry at the loop apex. The equations of motion for each particle j are given by

$$m_\alpha \ddot{x}_{j,\alpha} = eE\left(x_{j,\alpha}\right) + gm_\alpha \sin\left(\frac{\pi x_{j,\alpha}}{2L}\right), \tag{3.1}$$

where $x \in [-L, L]$ denotes the curvilinear coordinate along the loop. The self-consistent electric field[1] is expressed as

$$E(x) = 8\,\text{sign}(e_\alpha)e \cdot n_S N \sum_{n=1}^{N_n} \frac{Q_n}{n}\sin\left(\frac{\pi n x}{L}\right), \tag{3.2}$$

where $2N$ is the total number of particles of the species α, n_S is the surface number density and Q_n are the charge imbalance parameters defined as

$$Q_n = \sum_{\alpha \in \{e,i\}} \text{sign}(e_\alpha)q_{n,\alpha}, \tag{3.3}$$

with the stratification parameters $q_{n,\alpha}$ given by

$$q_{n,\alpha} = \frac{1}{N} \sum_{j=1}^{N} \cos\left(\frac{\pi n x_{j,\alpha}}{L}\right). \tag{3.4}$$

Physically, $q_{n,\alpha} \approx -1$ corresponds to particles concentrated near the base of the loop, $q_{n,\alpha} \approx 0$ to a uniform distribution and $q_{n,\alpha} \approx 1$ to particles clustered near the loop top. A non-zero Q_n implies a charge imbalance at spatial scale L/n. The Fourier components ρ_n of the charge density $\rho(x)$ are related to Q_n via the Poisson equation:

$$\frac{\partial^2 \phi}{\partial x^2} = -4\pi e\rho(x) \quad \rightarrow \quad \rho_n = -en_0 Q_n, \quad n_0 = \frac{Nn_S}{L}, \tag{3.5}$$

indicating that Q_n directly determines the spatial structure of the charge density at the spatial scale L/n.

The loop is assumed to be in ideal thermal contact with a lower boundary representing the fully collisional chromosphere. However, as discussed in §1, the upper chromosphere and the base of the transition region are highly dynamic environments, characterised by intense, short-lived and small-scale brightenings (Dere *et al.* 1989; Teriaca *et al.* 2004; Peter *et al.* 2014; Tiwari *et al.* 2019; Berghmans *et al.* 2021).

We model these brightenings as temperature pulses as illustrated in figure 2. When the boundary temperature is held constant, the loop plasma reaches thermal equilibrium (isothermal loop). However, the dynamic behaviour of the chromosphere introduces stochastic heating events, which are analysed in § 5.2.

---

[1]We note that the expression for the electrostatic field expanded in Fourier modes is general and applies in both the presence and absence of collisions. However, given that collisions are not included in the present model, we do not expect to recover (2.2) with all its terms. Furthermore, we point out that, unlike in the previous section, we are now working in the curvilinear coordinates of the loop, which are related to the height z through $z = (2L/\pi)\cos(\pi x/2L)$.
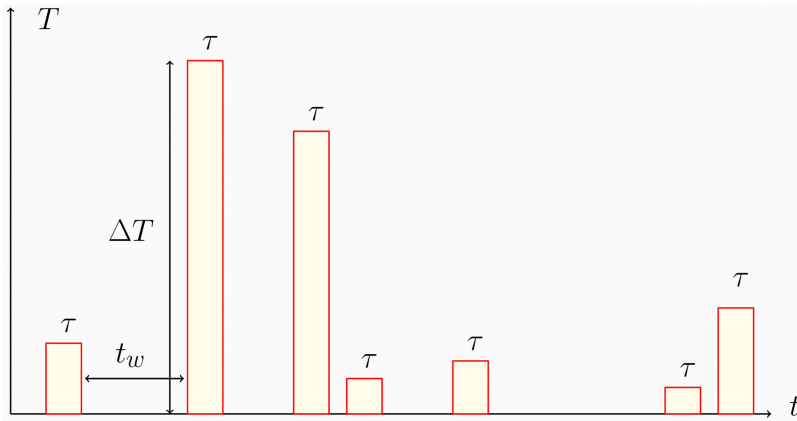
FIGURE 2. Time evolution of the temperature at the thermal boundary. During intervals of duration τ, the temperature is increased by an amount ΔT, while during the waiting times t_w, it is at the baseline value T_0.

3.1. *The system of units*

We now proceed to express the equations of motion in dimensionless form. We introduce characteristic units

$$v_0 = \sqrt{\frac{k_B T_0}{m_e}}, \quad m_0 = m_e, \quad L_0 = \frac{L}{\pi}, \tag{3.6}$$

and define the dimensionless variables

$$M = \frac{m_p}{m_e}, \quad C = \frac{8e^2 L^2 n_0}{\pi k_B T_0}, \quad \tilde{g} = \frac{gLm_p}{\pi k_B T_0}. \tag{3.7}$$

The quantities C and $\tilde{g}$ quantify the strength of the self-electrostatic energy and of the gravitational energy of the electrons in units of thermal energy. In these units, denoting with θ the dimensionless spatial coordinate, the equations of motion become

$$M_\alpha \ddot{\theta}_{j,\alpha} = \text{sign}(e_\alpha) E\left(\theta_{j,\alpha}\right) + \tilde{F}\left(\theta_{j,\alpha}\right), \tag{3.8}$$

the expressions for the external forces and the electrostatic field are

$$\tilde{F}\left(\theta_{j,\alpha}\right) = \tilde{g}_\alpha \sin\left(\frac{\theta_{j,\alpha}}{2}\right), \quad E(\theta) = C \sum_{n=1}^{N_n} \frac{Q_n}{n} \sin\left(n\theta\right) \tag{3.9}$$

and

$$Q_n = \sum_{\alpha \in \{p,e\}} \text{sign}(e_\alpha) q_{n,\alpha}, \quad q_{n,\alpha} = \frac{1}{N} \sum_{j=1}^{N} \cos\left(n\theta_{j,\alpha}\right). \tag{3.10}$$

In the aforementioned equations, M_α is equal to the mass ratio $M = m_p/m_e$ for protons and 1 for electrons, while $\tilde{g}_\alpha$ is equal to $\tilde{g}$ for protons and $\tilde{g}/M$ for electrons. Henceforth, all quantities are reported in dimensionless units unless specified otherwise.

3.2. *Vlasov dynamics*

In the mean-field limit, the dynamics of the phase-space distribution functions is governed by a system of two Vlasov equations:

$$\frac{\partial f_\alpha}{\partial t} + \frac{p}{M_\alpha}\frac{\partial f_\alpha}{\partial \theta} + F_\alpha[f_\alpha]\frac{\partial f_\alpha}{\partial p} = 0, \quad F_\alpha = -\frac{\partial H_\alpha}{\partial \theta}, \tag{3.11}$$

where f_α are the distribution functions for both species and H_α are the mean-field Hamiltonians:

$$H_\alpha = \frac{p^2}{2M_\alpha} + V_\alpha, \qquad V_\alpha(\theta) = \text{sign}(e_\alpha)\phi(\theta) + 2\tilde{g}_\alpha \cos\left(\frac{\theta}{2}\right). \tag{3.12}$$

Here ϕ is given by

$$\phi(\theta) = C\sum_{n=1}^{+\infty}\frac{Q_n}{n^2}\left(\cos(n\theta) + (-1)^{n+1}\right), \tag{3.13}$$

and Q_n are given by

$$Q_n[f_\alpha] = \sum_{\alpha\in\{e,p\}}\text{sign}(e_\alpha)q_{n,\alpha}[f_\alpha], \quad q_{n,\alpha}[f_\alpha] = \int_{-\pi}^{\pi}\mathrm{d}\theta\int_{-\infty}^{\infty}\mathrm{d}p\,\cos(n\theta)f_\alpha(\theta, p). \tag{3.14}$$

4. Reproducing the Pannekoek–Rosseland field and charge neutrality with the multi-mode model

In this section, we demonstrate that the multi-mode electrostatic interaction model is capable of reproducing both the Pannekoek–Rosseland potential and the charge neutrality condition in the limit of a large number of Fourier modes. According to Jeans' theorem, all stationary solutions of the Vlasov equation must depend solely on the mean-field Hamiltonians. Consequently, the distribution functions for each species can be expressed as

$$f_\alpha(\theta, p) = f_\alpha(H_\alpha). \tag{4.1}$$

By combining (4.1) with (3.14) we obtain

$$Q_n = \sum_{\alpha\in\{e,p\}}\text{sign}(e_\alpha)\int_{-\infty}^{+\infty}\mathrm{d}p\int_{-\pi}^{+\pi}\mathrm{d}\theta\,\cos(n\theta)f_\alpha(H_\alpha). \tag{4.2}$$

Using the kinetic definition of number density, (4.2) can be rewritten as

$$Q_n = \sum_{\alpha\in\{e,p\}}\text{sign}(e_\alpha)\int_{-\pi}^{+\pi}\mathrm{d}\theta\,\cos(n\theta)n_\alpha(V_\alpha), \tag{4.3}$$

where V_α is the total potential for each species. Since V_α depends on all Q_n, this results in a system of coupled nonlinear equations. In general, this system cannot be solved analytically for the number densities n_α, but an analytical solution can be obtained under broad assumptions. First, we assume that the functional form of the number density is identical for both species:

$$n_\alpha(V_\alpha) = n(V_\alpha). \tag{4.4}$$

This assumption is satisfied by several well-known distribution functions, including thermal distributions, kappa distributions (Scudder 1992*a*, *b*) and superstatistics (Beck & Cohen 2003), all widely used in theoretical modelling and observations of stellar atmospheres (Dudík *et al*. 2017; Lazar & Fichtner 2021; Barbieri *et al*. 2024*a*).

We now parametrise the Pannekoek–Rosseland potential along the loop's curvilinear coordinate θ as

$$\phi_{\mathrm{PR}}(\theta) = \sum_{\alpha \in \{e,p\}} \operatorname{sign}(e_\alpha) \frac{\tilde{g}_\alpha}{2} \cos\left(\frac{\theta}{2}\right), \tag{4.5}$$

which can be expanded in a Fourier series as

$$\phi_{\mathrm{PR}}(\theta) = \sum_{k=0}^{+\infty} c_k \cos(k\theta), \quad c_k = \sum_{\alpha \in \{e,p\}} \operatorname{sign}(e_\alpha) \tilde{g}_\alpha \frac{(-1)^k}{(1-4k^2)}. \tag{4.6}$$

The Pannekoek–Rosseland potential can be reproduced by the electrostatic interactions if the following condition holds:

$$C \sum_{n=1}^{N_n} \frac{Q_n}{n^2} \left(\cos(n\theta) + (-1)^{n+1}\right) = \sum_{k=0}^{+\infty} c_k \cos(k\theta). \tag{4.7}$$

This can be rewritten as

$$C \left(\sum_{n=1}^{N_n} \frac{Q_n}{n^2} \cos(n\theta) + Q_0\right) = \sum_{k=0}^{+\infty} c_k \cos\left(\frac{\pi k x}{L}\right), \qquad Q_0 = \frac{(-1)^n Q_n}{n^2}. \tag{4.8}$$

This condition is satisfied only if the number of Fourier modes $N_n \to +\infty$, and the Q_n coefficients satisfy

$$Q_n = C_q \frac{n^2 (-1)^n}{(1-4n^2)}, \quad C_q = \frac{1}{C} \sum_{\alpha \in \{e,p\}} \operatorname{sign}(e_\alpha) \tilde{g}_\alpha. \tag{4.9}$$

This ensures that the electrostatic potential matches the Pannekoek–Rosseland potential exactly. Furthermore, if (4.4) is satisfied, then the right-hand side of (4.3) vanishes, implying $Q_n = 0 \ \forall n$. However, (4.9) shows that $Q_n \neq 0$, unless C_q is negligible.

For typical coronal plasma conditions (e.g. $2L \sim 60$ Mm, $n_0 \sim 10^9$ cm^{-3}, $T_0 = 10^6$ K), we find $C_q \sim 10^{-20}$, which justifies the approximation $Q_n \sim 0$, and hence the quasi-neutrality condition is satisfied. The coefficients Q_n are related to the Fourier modes of the charge density $\rho(x)$ through (3.5). Since $|Q_n| \to C_q/4$ for large n, the Fourier series of $\rho(x)$ diverges unless it is truncated at a finite mode $\hat{n}$, satisfying

$$\hat{n} Q_{\hat{n}} \sim 1 \quad \text{and} \quad \hat{n} \gg 1, \tag{4.10}$$

leading to

$$\hat{n} \sim 4/C_q \quad \forall n < \hat{n}. \tag{4.11}$$

Now, since $C_q \sim 10^{-20}$, for (4.11) we have that $\hat{n} \sim 4 \times 10^{20}$. This implies that the solution of the system of (4.9) is given by (4.3) up to $n < \hat{n}$. Now, since $Q_n \sim 0$ for

all $n < \hat{n}$, and given that the charge density components ρ_n are proportional to Q_n via (3.5), it follows that $\rho_n \sim 0$ for all $n < \hat{n}$ as well.

In conclusion, we have shown that electrostatic interactions can reproduce the Pannekoek–Rosseland potential and enforce quasi-neutrality down to a very small spatial scale proportional to $L/\hat{n}$, in the realistic limit where electrostatic forces dominate over gravity, i.e. $C_q \ll 1$. This behaviour appears to be general and not limited to loop geometry, as further demonstrated in Appendix A for a plane-parallel atmosphere. Now a natural question arises: where does this electric field come from?

To investigate where any residual charge imbalance occurs, we consider the case $C_q \sim 400$, implying $\hat{n} = 100$ according to (4.11). The electrostatic potential is then approximated by

$$\phi(\theta) \cong \sum_{k=0}^{\hat{n}} c_k \cos(k\theta), \qquad (4.12)$$

and the total charge density becomes

$$\rho(\theta) \cong -\sum_{n=1}^{\hat{n}} Q_n \cos(n\theta). \qquad (4.13)$$

Figure 3 illustrates that the self-consistent electrostatic potential (blue) closely approximates the Pannekoek–Rosseland potential (grey) throughout the loop. The middle panel shows that the discrepancies are more pronounced near the base of the loop. These differences are associated with a localised charge imbalance, as depicted in the right-hand panel. This analysis indicates that the Pannekoek–Rosseland potential primarily arises from a thin charge layer at the base of the loop, while the upper regions remain approximately quasi-neutral. This outcome is anticipated, as the gravitational force attains its maximum at the base, whereas the electrostatic field vanishes at that point.

5. Validation of the multi-mode electrostatic model

In the previous section, we demonstrated that under the following assumptions:

(i) the number density satisfies $n_\alpha(V_\alpha) = n(V_\alpha)$,

(ii) the parameter $C_q \ll 1$, that is, electrostatic interactions are much stronger than gravitational forces,

the multi-mode electrostatic model increasingly approximates charge neutrality and the Pannekoek–Rosseland potential as the number of Fourier modes increases. We now validate this conclusion for different types of distribution functions.

5.1. *Thermal solution for multi-mode models*

Among all the stationary solutions of the Vlasov equation, the thermal solution is given by

$$f_\alpha(H_\alpha) = \frac{1}{Z_\alpha} e^{-H_\alpha/T} \quad \text{and} \quad Z_\alpha = \int_{-\infty}^{+\infty} dp \int_{-\pi}^{\pi} d\theta\, e^{-H_\alpha/T}, \qquad (5.1)$$

where Z_α is the partition function.

Using the standard kinetic definitions, the number density for each species becomes

$$n_\alpha(\theta) = n(V_\alpha) = \frac{e^{-V_\alpha(\theta)/T}}{\int_{-\pi}^{\pi} d\theta\, e^{-V_\alpha(\theta)/T}}. \qquad (5.2)$$
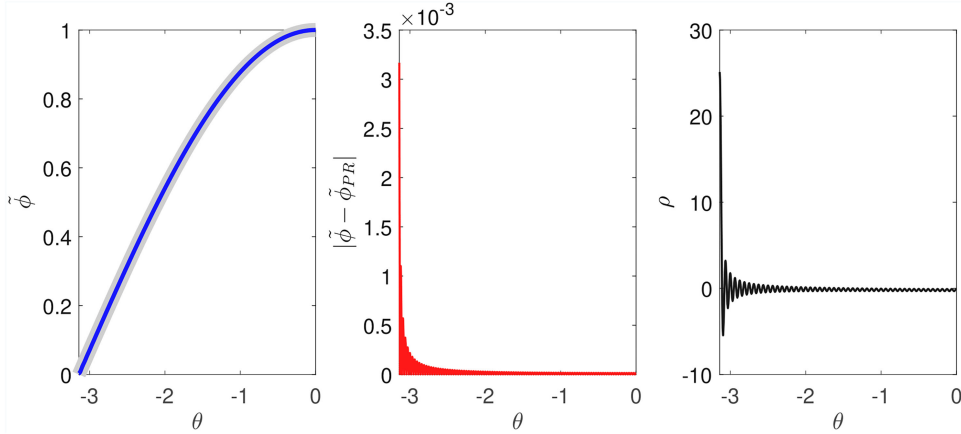
FIGURE 3. Left: the self-consistent electrostatic potential ϕ (blue) and the Pannekoek–Rosseland potential ϕ_{PR} (grey), plotted as functions of the curvilinear coordinate θ, both normalised by the factor $\sum_{\alpha \in \{e, p\}} \text{sign}(e_\alpha)\tilde{g}_\alpha$. The resulting rescaled potentials are denoted as $\tilde{\phi}$ and $\tilde{\phi}_{PR}$, respectively. The self-consistent potential is computed from (4.12), while the Pannekoek–Rosseland potential is obtained from (4.5). Centre: the absolute difference $|\tilde{\phi} - \tilde{\phi}_{PR}|$ as a function of θ, highlighting the spatial deviation between the two potentials. Right: the charge density $\rho(\theta)$ plotted as a function of θ, calculated using (4.13).

From this expression, it is evident that thermal distributions satisfy the density condition in (4.4). Substituting (5.2) into (4.3) and performing some algebra yields

$$Q_n = \sum_{\alpha \in \{e, p\}} \text{sign}(e_\alpha) \frac{\int_{-\pi}^{0} d\theta \cos(n\theta) e^{-V_\alpha(\theta)/T}}{\int_{-\pi}^{0} d\theta e^{-V_\alpha(\theta)/T}}. \tag{5.3}$$

Solving this nonlinear system provides the values of $Q_n \; \forall n$. To ensure the recovery of charge neutrality and the Pannekoek–Rosseland potential, the condition $C_q \ll 1$ must be satisfied.

Figure 4 presents the numerical results obtained with dimensionless parameters satisfying $C_q \ll 1$, specifically: $\tilde{g} = 32$, $M = m_p/m_e$, $C = 10^4$, $T = 90$. The left-hand panels show the electron (red) and proton (blue) number density profiles computed via (5.2), where the coefficients Q_n are derived by solving (5.3) using $N_n = 1$ (top row), $N_n = 2$ (middle row) and $N_n = 9$ (bottom row) Fourier modes. The grey curves represent the density profiles computed using the Pannekoek–Rosseland potential from (4.5). As the number of Fourier modes increases, the species densities converge towards the Pannekoek–Rosseland profile, indicating improved charge neutrality. The right-hand panels of figure 4 show the corresponding electrostatic potential computed from (3.13) (blue), alongside the Pannekoek–Rosseland potential (grey). The convergence of the self-consistent potential towards the Pannekoek–Rosseland solution with increasing N_n confirms the analytical predictions of § 4.

5.1.1. *Validation via numerical simulations*
We now demonstrate that the dynamic model introduced in § 3 relaxes towards the thermal equilibrium configuration described above, provided that the thermal
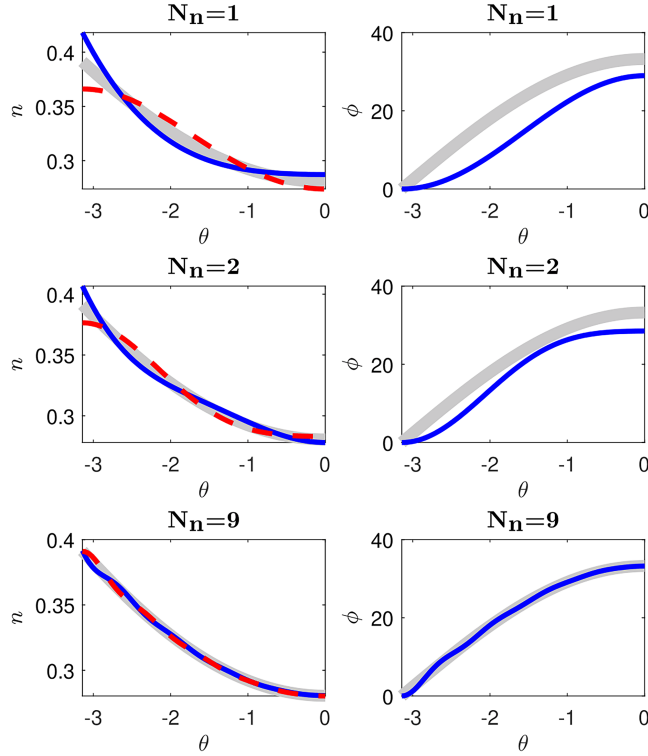
FIGURE 4. Top row, left-hand panel: electron (red) and proton (blue) number densities as functions of the curvilinear coordinate along the loop. The densities are computed using (5.2) with a single Fourier mode ($N_n = 1$), as indicated in the subplot title. The grey curve shows the reference density profile corresponding to the Pannekoek–Rosseland potential. Top row, right-hand panel: the Pannekoek–Rosseland potential (grey), calculated using (2.3), and the self-consistent electrostatic potential (blue), computed using (3.13) with one Fourier mode. Middle and bottom rows: same as the top row, but for $N_n = 2$ and $N_n = 9$, respectively.

boundary is held at a constant temperature T. We initialise the system with isothermal distributions for both electrons and protons, accounting for their respective gravitational stratifications:

$$f_\alpha(\theta, p) = \frac{e^{-(1/T)(p^2/(2M_\alpha) + 2\tilde{g}_\alpha \cos(\theta/2))}}{\sqrt{2\pi M_\alpha T} \int_{-\pi}^{\pi} d\theta e^{-(2\tilde{g}_\alpha/T)\cos(\theta/2)}}. \tag{5.4}$$

This configuration is not dynamically stable, as it yields distinct stratifications for the two species. As a result, an ambipolar electric field emerges and progressively acts to equalise the species densities, enforcing charge neutrality. This effect can only be reproduced if a sufficient number of Fourier modes is included in the electrostatic model.

We integrate numerically (3.8)[2] using $N_n = 9$ modes and the same parameter values as in figure 4, for $N = 2^{17}$ particles. The top-left panel of figure 5 shows the

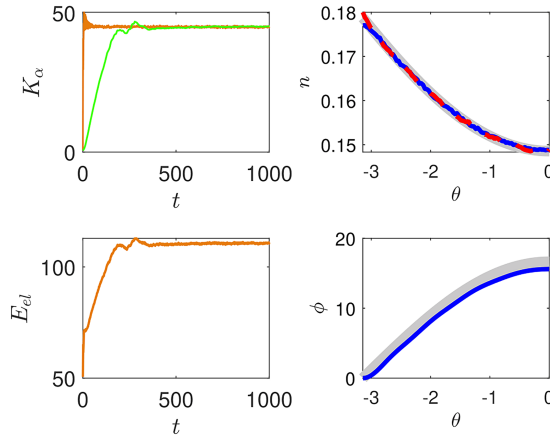[2]The details of the numerical approach are explained in Barbieri *et al.* (2024*b*).

FIGURE 5. Top left: time evolution of the kinetic energies K_α of protons (green curve) and electrons (orange curve). Top right: number densities of electrons (blue) and protons (red). The grey curves correspond to the theoretical density profile obtained from (5.2), where the electrostatic potential ϕ is replaced by the Pannekoek potential given in (4.5). Bottom left: time evolution of the total electrostatic energy E_{el}, evaluated numerically via (5.6). Bottom right: self-consistent electrostatic potential ϕ, computed from simulations using (3.13). The grey curve represents the Pannekoek potential given by (4.5).

time evolution of the kinetic energies of electrons (orange) and protons (green), defined as

$$K_\alpha = \frac{1}{N} \sum_{j=1}^{N} \frac{p_{j,\alpha}^2}{2M_\alpha}. \tag{5.5}$$

Both kinetic energies relax to an asymptotic value, consistent with thermal equilibrium. In this state, the electron and proton densities coincide and match the Pannekoek–Rosseland density profile (grey), shown in the top-right panel. The bottom-left panel illustrates the time evolution of the total electrostatic energy:

$$E_{el} = \frac{C}{2} \sum_{n=1}^{N_n} \frac{Q_n^2}{n^2}. \tag{5.6}$$

This quantity also relaxes to an asymptotic value. The electrostatic potential corresponding to this asymptotic state (blue), shown in the bottom-right panel, closely matches the Pannekoek–Rosseland potential (grey), confirming the model's ability to self-consistently reproduce the equilibrium solution.

5.2. *Multi-temperature solution for multi-mode models*

The thermal solution presented above is valid under the assumption of a static thermal boundary at fixed temperature T. However, as discussed in § 3 as well as in § 1, our primary interest lies in the case where the thermal boundary exhibits time-dependent temperature fluctuations. As shown in Barbieri *et al.* (2024*b*), if the time scales of these fluctuations are shorter than the relaxation time of the loop at each corresponding temperature, then the system relaxes towards a non-equilibrium stationary state. In this regime, the distribution functions of the plasma particles are

described by the following analytical expression:

$$f_\alpha (\theta, p) = \mathcal{N}_\alpha \left(A \int_1^{+\infty} dT \frac{\gamma(T)}{T} e^{-H_\alpha/T} + (1-A) e^{-H_\alpha} \right), \quad A = \frac{\tau}{\tau + \langle t_w \rangle_\eta}, \quad (5.7)$$

where $\mathcal{N}_\alpha$ is the normalisation constant ensuring that f_α integrates to unity, $\gamma(T)$ is the probability distribution of the temperature increments, τ is the duration of the heating events and $\langle t_w \rangle$ is the average waiting time between events over the probability distribution $\eta(t_w)$. Using the standard kinetic definitions, we compute the number density and kinetic temperature for each species:

$$n_\alpha (\theta) = n (V_\alpha) = \frac{A \int_1^{+\infty} dT \gamma(T)/\sqrt{T} e^{-V_\alpha/T} + (1-A) e^{-V_\alpha}}{A \int_1^{+\infty} dT \gamma(T)/\sqrt{T} \int_{-\pi}^{\pi} d\theta e^{-V_\alpha/T} + (1-A) \int_{-\pi}^{\pi} d\theta e^{-V_\alpha}}, \quad (5.8)$$

$$T_\alpha (\theta) = T (V_\alpha) = \frac{A \int_1^{+\infty} dT \gamma(T)/\sqrt{T} e^{-V_\alpha/T} + (1-A) e^{-V_\alpha}}{A \int_1^{+\infty} dT \gamma(T)/\sqrt{T} e^{-V_\alpha/T} + (1-A) e^{-V_\alpha}}. \quad (5.9)$$

These multi-temperature distributions also satisfy the condition given by (4.4), required for the system to approach charge neutrality. By inserting (5.8) into the system of (4.3), and after some manipulation, we obtain

$$Q_n = \sum_{\alpha \in \{e, p\}} \text{sign} (e_\alpha)$$

$$\times \frac{A \int_1^{+\infty} dT (\gamma(T)/\sqrt{T}) \int_{-\pi}^0 d\theta \cos(n\theta) e^{-V_\alpha/T} + (1-A) \int_{-\pi}^0 d\theta \cos(n\theta) e^{-V_\alpha}}{A \int_1^{+\infty} dT \gamma(T)/\sqrt{T} \int_{-\pi}^0 d\theta e^{-V_\alpha/T} + (1-A) \int_{-\pi}^0 d\theta e^{-V_\alpha}}.$$
$$(5.10)$$

Solving this system yields the values of Q_n for all modes. As with the thermal case, we demonstrate this behaviour using dimensionless parameters that satisfy the condition $C_q \ll 1$. The results are shown in figure 6, where we assume a delta-distribution for the temperature increments,

$$\gamma(T) = \delta(T - (1 + \Delta T)), \quad (5.11)$$

corresponding to a boundary temperature that alternates between two discrete values. The chosen parameters are: $A = 0.1$, $\tilde{g} = 2$, $M = m_p/m_e$, $C = 10^4$, $\Delta T = 90$. In figure 6, the left-hand panels display the temperature and number density profiles of electrons (blue) and protons (red dashed), computed from (5.8) and (5.9), respectively, using $N_n = 1, 2, 9$. The grey lines represent the profiles obtained using the Pannekoek–Rosseland potential. As in the thermal case, increasing the number of Fourier modes leads to convergence of the electron and proton profiles towards the Pannekoek–Rosseland solutions, indicating that charge neutrality and the correct electrostatic potential structure are recovered. The right-hand panels show the corresponding electrostatic potentials computed using (3.13) (blue) compared with the Pannekoek–Rosseland potential (grey). Once again, convergence is observed as the number of modes increases. In Appendix B we show a case in which $\gamma(T)$ is not a simple delta-distribution proving the robustness of the present result.

5.2.1. Validation against numerical simulations
The dynamics governed by the equations of motion (3.1), coupled with the fluctuating thermal boundary, has been numerically simulated following the methodology
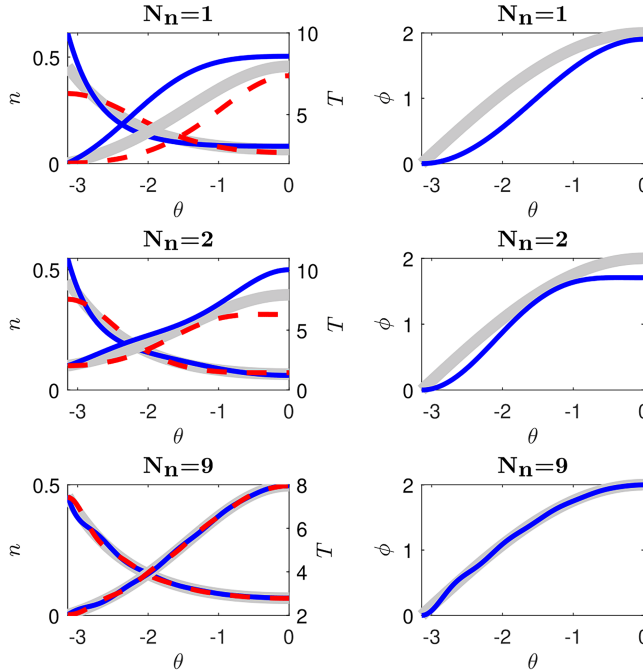
FIGURE 6. Top row, left-hand panel: electron (red) and proton (blue) number densities (globally decreasing functions) and temperatures (globally increasing functions) as functions of the curvilinear coordinate along the loop. The densities and temperature are computed using (5.2) with a single Fourier mode ($N_n = 1$), as indicated in the subplot title. The grey curve shows the reference temperature and density profiles corresponding to the Pannekoek–Rosseland potential. Top row, right-hand panel: the Pannekoek–Rosseland potential (grey), calculated using (2.3), and the self-consistent electrostatic potential (blue), computed using (3.13) with one Fourier mode. Middle and bottom rows: same as the top row, but for $N_n = 2$ and $N_n = 9$, respectively.

described in Barbieri *et al.* (2024*a*, *b*), with the notable difference that the electric field is computed using (3.2). In this section, we illustrate how the fluctuating thermal boundary drives the overlying collisionless plasma towards a stationary state characterised by a temperature inversion. To this end, the system is initialised in a thermal equilibrium configuration, in which the distribution functions for both species are given by

$$f_\alpha (\theta, p) = \frac{e^{-p^2/(2M_\alpha)-2\tilde{g}\cos(\theta/2)}}{\sqrt{2\pi M_\alpha} \int_{-\pi}^{\pi} d\theta\, e^{-2\tilde{g}\cos(\theta/2)}} \quad \forall \alpha. \tag{5.12}$$

This configuration is not stationary under the influence of the dynamically fluctuating thermal boundary at the base. However, as discussed in § 3, if a sufficiently large number of Fourier modes is retained in the modelling of the self-consistent electrostatic interactions, we expect the system to recover both charge neutrality and the Pannekoek–Rosseland potential in the stationary state. We report here the results of a simulation conducted with $N_n = 9$ modes and using the same set of numerical parameters employed for the production of figure 6. The total number of particles is set to $N = 2^{17}$. In analogy with figure figure 5, the upper-left panel
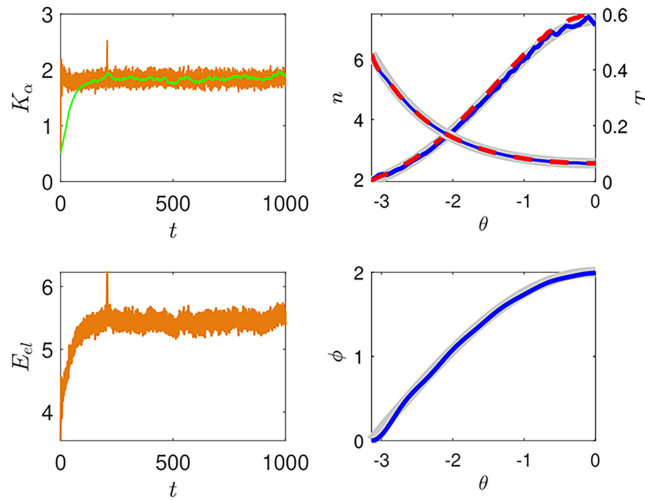
FIGURE 7. Same quantities and colour scheme as in figure 5, but in the multi-temperature case regime described in § 5.2.

of figure 7 shows the time evolution of the total kinetic energy of each species α, computed according to (5.5). In this case as well, the kinetic energies of both species relax towards an asymptotic value. The upper-right panel displays the final stationary profiles of temperature and density computed via the numerical simulation together with their theoretical counterparts, which clearly exhibit a temperature inversion. The theoretical profiles, shown in grey, are computed using (5.8) and (5.9), where the electrostatic potential $\phi(\theta)$ is replaced by the Pannekoek–Rosseland expression given in (4.5). The lower-left panel illustrates the time evolution of the total electrostatic energy, evaluated using (5.6). As observed in the case discussed in § 5.1, this quantity also relaxes to an asymptotic value. Finally, the lower-right panel confirms that the self-consistent electrostatic potential generated by the plasma coincides with the Pannekoek–Rosseland potential at equilibrium.

6. Summary and perspectives

The main plasma physics result of the present work is the identification of a self-consistent mechanism to reproduce the ambipolar effect that gives rise to the Pannekoek–Rosseland electric field and ensures charge neutrality in a gravitationally stratified, collisionless plasma. This is achieved by extending the electrostatic interaction model from a single Fourier mode (as in the standard HMF approximation) to multiple modes. Under very general assumptions on the form of the distribution functions, assumptions that are satisfied by thermal, kappa and superstatistical distributions, we demonstrated that in the limit of many modes, the self-consistent electrostatic potential converges to the classical Pannekoek–Rosseland potential. At the same time, the system exhibits quasi-neutrality apart from a thin layer of charge at the base of the atmosphere which originates the Pannekoek–Rosseland potential. These theoretical predictions were confirmed numerically. We have shown that, under suitable conditions, the distribution functions of both species relax towards a stationary configuration in which charge neutrality and the Pannekoek–Rosseland potential are simultaneously recovered. This was observed both in the

thermal equilibrium case (where the boundary temperature is fixed) and in the more physically relevant multi-temperature case, where the thermal boundary undergoes random energy fluctuations.

While the results of this work do not aim to provide a general theory of ambipolar electric fields nor a complete description of coronal heating, they represent a foundational step in that direction. Now that we have established how to incorporate the ambipolar effect in a self-consistent way into the model originally introduced in Barbieri *et al*. (2024*a*, *b*), we are in a position to extend it. In particular, we can include additional ingredients such as collisions, ionisation processes and asymmetric temperature fluctuations at the loop footpoints. These effects will allow us to determine how the ambipolar electric field predicted by the multi-mode Fourier approach is modified, and how the picture of coronal heating evolves in this more complete framework.

As discussed in § 2, we expect collisions to modify the self-generated electric field with respect to the classical Pannekoek–Rosseland expression. For example, we aim to investigate the following questions: How many Fourier modes are required to reproduce the modified ambipolar field in the collisional case? In which regions of the atmosphere are the deviations from the Pannekoek–Rosseland field most significant? How does this modified electric field act on the temperature inversion produced by gravitational filtering in the collisionless limit? Finally, by including collisions, we can study the interplay between the collisionless gravitational filtering, which produces the temperature inversion effect, and the collisional thermal conduction, which allows heat to flow from the corona into the chromosphere.

Another important extension of the present model concerns the role of partial ionisation, especially in the lower part of the transition region, where the ionisation process is known to occur. In this regime, deviations from the classical Pannekoek–Rosseland field may become more significant, as the plasma is not yet fully ionised. As altitude increases and ionisation progresses, the assumptions of a fully ionised and collisionless plasma, underlying the present treatment, become more accurate. Understanding how the ambipolar electric field evolves across this ionisation gradient represents an important development of our model.

We note that in our model we have central symmetry with respect to the loop apex. This will ensure a zero net flux in the system. By introducing asymmetric temperature fluctuations at the two footpoints, a net flux across the loop appears.

However, the resulting asymmetry does not alter the physical mechanism responsible for the temperature inversion. The inversion still arises because 'hot' particles, generated by temperature increments, can climb higher in the gravitational potential well, while 'cold' particles remain concentrated near the base and the temperature profile along the loop is no longer symmetric. Although this adds complexity to the model, it does not change the physical origin of the temperature inversion. It represents an interesting extension that we plan to explore in a future work.

We note that generating different temperature increments at the two footpoints of the loop produces a flow into the system, altering the ambipolar electric field, which would no longer be the classical Pannekoek–Rosseland field. Another way to obtain a different ambipolar field could be through the introduction of distinct temperature fluctuations for the two species. This leads to different temperature profiles for electrons and protons, and consequently, as evident from (2.2), an ambipolar electric field that deviates from the classical Pannekoek–Rosseland expression.

Finally, as an additional possible follow-up, it would be interesting to include alpha particles in the modelling, as they contribute significantly to the mass density.

Acknowledgements

Editor Francesco Califano thanks the referees for their advice in evaluating this article.

Funding

Declaration of interests

The author reports no conflict of interest.

Appendix A. Plane-parallel plasma atmosphere

In this appendix, we adopt the CGS system of units. We consider a model of a two-component, plane-parallel, collisionless plasma atmosphere. Particles are subject both to the gravitational field of the central star and to self-consistent electrostatic interactions. Under these assumptions, the distribution functions f_α evolve according to the Vlasov equations:

$$\frac{\partial f_\alpha}{\partial t} + \frac{p}{m_\alpha}\frac{\partial f_\alpha}{\partial z} + F_\alpha[f_\alpha]\frac{\partial f_\alpha}{\partial p} = 0, \quad F_\alpha = -\frac{\partial H_\alpha}{\partial z}, \quad H_\alpha = \frac{p^2}{2m_\alpha} + V_\alpha. \tag{A1}$$

The total potential is defined as

$$V_\alpha(z) = \text{sign}(e_\alpha)\phi(z) + m_\alpha g z, \tag{A2}$$

with $\phi(z)$ being the electrostatic potential, which satisfies the Poisson equation:

$$\frac{\mathrm{d}^2\phi}{\mathrm{d}z^2} = -4\pi e\rho(z). \tag{A3}$$

Using the Green's function formalism, the electrostatic potential can be expressed as

$$\phi(z) = -2\pi e^2 n_0 \sum_{\alpha\in\{e,p\}} \int_0^L \mathrm{d}\tilde{z}\, n_\alpha(z)|z - \tilde{z}|, \tag{A4}$$

where L is the extent of the atmosphere. Assuming that the distribution functions depend only on the Hamiltonians (the Jeans theorem), and making the same assumptions as in (4.4), we obtain

$$\phi(z) = -2\pi e^2 n_0 \sum_{\alpha\in\{e,p\}} \int_0^L \mathrm{d}\tilde{z}\, n(V_\alpha)|z - \tilde{z}|. \tag{A5}$$

Introducing the dimensionless coordinate $y = z/L$, we rewrite the expression as

$$\frac{\phi(z)}{2\pi e^2 n_0 L^2} = \sum_{\alpha\in\{e,p\}} \int_0^1 \mathrm{d}\tilde{y}\, n(V_\alpha)|y - \tilde{y}|. \tag{A6}$$

We parametrise the Pannekoek–Rosseland field in this geometry:

$$\phi_{\mathrm{PR}}(z) = \sum_{\alpha \in \{e,p\}} \mathrm{sign}(e_\alpha) m_\alpha g z. \tag{A7}$$

Substituting $\phi(z) = \phi_{\mathrm{PR}}(z)$ into the integral equation above, we find that the right-hand side of (A6) vanishes, while the left-hand side yields $2C_q y$, which is not identically zero. However, under typical plasma conditions where $C_q \ll 1$, and for $y \in [0, 1]$, the deviation is negligible, confirming the validity of the approximation.

Appendix B. The case of a statistical distribution of the temperature increments

In this appendix, we consider the case where the temperature increments follow a statistical distribution. In particular, as previously done in Barbieri *et al.* (2024*a*, *b*) and Barbieri *et al.* (2025), we adopt an exponential distribution for the temperature increments:

$$\gamma(T) = \frac{1}{\langle \Delta T \rangle} \mathrm{e}^{-(T-T_0)/\langle \Delta T \rangle}, \quad T > T_0. \tag{B1}$$

We solve (5.10) using the distribution $\gamma(T)$ defined above. Once the coefficients Q_n are obtained, we use the same statistical distribution to compute the temperature and density profiles via (5.9) and (5.8), respectively. Figure 8 presents the results for the following parameter values: $\tilde{g} = 2$, $M = m_p/m_e$, $C = 10^4$, $\langle \Delta T \rangle = 90$. As observed in the isothermal and multi-temperature cases discussed in §§ 5.1 and 5.2, respectively, the electrostatic interaction, when modelled with a sufficiently large number of Fourier modes, produces an electrostatic potential that closely approximates the
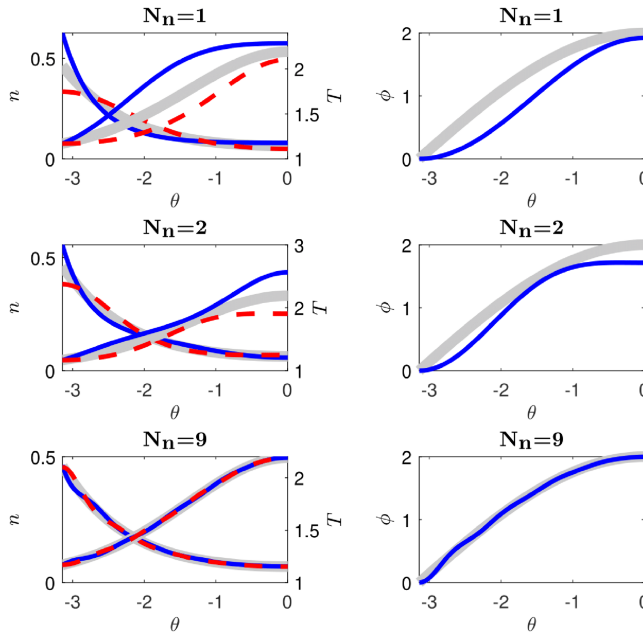

FIGURE 8. Same quantities as for figure 6 but computed via the statistical distribution of temperature increments given by (B1).

Pannekoek–Rosseland potential. This approach ensures quasi-neutrality by aligning the temperature and density profiles of electrons and protons across the entire loop.

REFERENCES

ANTONI, M. & RUFFO, S. 1995 Clustering and relaxation in hamiltonian long-range dynamics. *Phys. Rev. E* **52**, 2361–2374.

ASCHWANDEN, M.J. 2005 Physics of the solar corona. In *An Introduction with Problems and Solutions*, 2nd edn. Springer.

BARBIERI, C.L., ANDREA, V. & SIMONE, L. 2025 Temperature and density profiles in the corona of main-sequence stars induced by stochastic heating in the chromosphere. *Astron. Astrophys.* **694**, A154.

BARBIERI, L., CASETTI, L., VERDINI, A. & LANDI, S. 2024a Temperature inversion in a gravitationally bound plasma: case of the solar corona. *A& A* **681**, L5.

BARBIERI, L., PAPINI, E., DI, C., PIERFRANCESCO, L., SIMONE, V., Andrea, & CASETTI, L. 2024b Temperature inversion in a confined plasma atmosphere: coarse-grained effect of temperature fluctuations at its base. *J. Plasma Phys.* **90**, 905900511.

BECK, C. & COHEN, E. G. D. 2003 Superstatistics. *Phys. A: Stat. Mech. Appl.* **322**, 267–275.

BERGHMANS, D., *et al.* 2021 Extreme-UV quiet Sun brightenings observed by the solar orbiter/EUI. *Astron. Astrophys.* **656**, L4.

CHAVANIS, P. H., VATTEVILLE, J. & BOUCHET, F. 2005 Dynamics and thermodynamics of a simple model similar to self-gravitating systems: the HMF model. *Eur. Phys. J. B* **46**, 61–99.

DE PONTIEU, B., MCINTOSH, S.W., CARLSSON, M., HANSTEEN, V.H., TARBELL, T.D., BOERNER, P., MARTINEZ-SYKORA, J. & SCHRIJVER, C.J. 2011 *The origins of hot plasma in the solar corona. Science* **331**, 55.

DERE, K. P., BARTOE, J. D. F. & BRUECKNER, G. E. 1989 Explosive events in the solar transition zone. *Sol. Phys.* **123**, 41–68.

DMITRUK, P. & GOMEZ, D.O. 1997 Turbulent coronal heating and the distribution of nanoflares. *Astrophys. J. Lett.* **484**, L83.

DUDÍK, J., POLITO, V., DZIFČÁKOVÁ, E., ZANNA, G.D. & TESTA, P. 2017 Non-Maxwellian analysis of the transition-region line profiles observed by the interface region imaging spectrograph. *Astrophys. J.* **842**, 19.

ELSKENS, Y. & ESCANDE, D. 2019 Microscopic dynamics of plasmas and chaos.

RAPPAZZO, A.F., VELLI, M., EINAUDI, G. & DAHLBURG, R.B. 2008 Nonlinear dynamics of the parker scenario for coronal heating. *Astrophys. J.* **677**, 1348.

GUDIKSEN, B.V. & Nordlund 2005 An Ab initio approach to the solar coronal heating problem. *Astrophys. J.* **618**, 1020–1030.

HAU, L.-N., CHANG, C.-K., LAZAR, M. & POEDTS, S. 2025 Boltzmann–Poisson theory of nonthermal self-gravitating gases, cold dark matter, and solar atmosphere. *Astrophys. J.* **981**, 18.

HEYVAERTS, J. & PRIEST, E. R. 1983 Coronal heating by phase-mixed shear Alfven waves. *Astron. Astrophys.* **117**, 220–234.

HOWSON, T. A., DE MOORTEL, I. & REID, J. 2020 Phase mixing and wave heating in a complex coronal plasma. *Astron. Astrophys.* **636**, A40.

IONSON, J. A. 1978 Resonant absorption of Alfvénic surface waves and the heating of solar coronal loops. *Astrophys. J.* **226**, 650–673.

LANDI, S. & PANTELLINI, F. G. E. 2001 On the temperature profile and heat flux in the solar corona: kinetic simulations. *A&A* **372**, 686–701.

LAZAR, M. & FICHTNER, H. 2021 Kappa distributions: from observational evidences via controversial predictions to a consistent theory of nonequilibrium plasmas. In *Astrophysics and Space Science Library*. Springer.

PANNEKOEK, A. 1922 Ionization in stellar atmospheres (Errata: 2 24). *Bull. Astr. Inst. Netherlandd* **1**, 107.

PARKER, E. N. 1972 Topological dissipation and the small-scale fields in turbulent gases. *Astrophys. J.* **174**, 499.

PETER, H., *et al.* 2014 Hot explosions in the cool atmosphere of the Sun. *Science* **346**, 1255726.

RAPPAZZO, A. F. & PARKER, E. N. 2013 Current sheets formation in tangled coronal magnetic fields. *Astrophys. J.* **773**, L2.

ROSSELAND, S. 1924 Electrical state of a star. *MNRAS* **84**, 720–728.

SCUDDER, J.D. 1992*a* On the causes of temperature change in inhomogeneous low-density astrophysical plasmas. *Astrophys. J.* **398**, 299.

SCUDDER, J.D. 1992*b* Why all stars should possess circumstellar temperature inversions. *Astrophys. J.* **398**, 319.

TERIACA, L., BANERJEE, D., FALCHI, A., DOYLE, J. G. & MADJARSKA, M. S. 2004 Transition region small-scale dynamics as seen by SUMER on SOHO. *Astron. Astrophys.* **427**, 1065–1074.

TIWARI, S.K., *et al.* 2019 Fine-scale explosive energy release at sites of prospective magnetic flux cancellation in the core of the solar active region observed by Hi-C 2.1, IRIS, and SDO. *APJ* **887**, 56.

WILMOT-SMITH, A. L. 2015 An overview of flux braiding experiments. *Philos. Trans. R. Soc. Lond. Ser. A* **373**, 20140265.